

# High Resolution Imaging by Employing Passive and Active Approaches

Swapan K. Saha

*Indian Institute of Astrophysics, Bangalore - 560 034, India*

## 1. Introduction

The Earth's atmosphere is a highly turbulent medium that distorts the characteristics of downward propagating light; the longer the path, the more it suffers deflection. Light reaching the entrance pupil of an imaging system is coherent only within patches of diameter,  $\approx r_0$ — Fried's parameter [1]. This causes blurring of the image which limits the theoretical performance of any terrestrial large optical telescope as against lone orbiting one. The blurring suffered by such an image is modeled by a convolution with a point spread function (PSF).

The diffraction limited resolution of celestial objects viewed through such turbulence could be achieved by employing post-detection processing of a large data set of short exposure images using Fourier domain methods. Certain specialized moments of the Fourier transform of a short exposure image contain diffraction limited information about the object of interest. In a classic paper, Labeyrie [2] suggested a method called, speckle interferometry, where post-detection data processing algorithms are required to decipher diffraction limited spatial Fourier spectrum and image features of stellar objects. Though it is a passive approach, this method has opened up a new era in modern optics and has made impacts in several important fields in astrophysics [3, 4], viz., (i) in studying the separation and orientation of close binary stars [5], (ii) in measuring diameter of giant stars [6, 7], (iii) in resolving Pluto-Charon system [8], (iv) in determining shapes of asteroids [9], (v) in mapping the finer features of extended objects [10], (vi) in estimating sizes and mapping certain types of circumstellar envelopes [11, 12], (vii) in revealing structures of active galactic nuclei [13], and of compact clusters of a few stars like R136a complex [14], (viii) in resolving the gravitationally lensed QSO's [15], etc.

Following its success, astronomers focussed their efforts on developing post-detection image processing techniques and applied them to improve the resolution of astronomical images [3, 4]. Considerable amount of new informations have also come in by employing various other avenues at the telescopes, namely, (i) speckle spectroscopy, (ii) speckle polarimetry, (iii) shear interferometry, (iv) phase closure method, (v) aperture synthesis technique, (vi) differential speckle interferometry, (vii) phase diversity imaging etc. An interesting result from the speckle spectroscopic observations of a binary system,  $\phi$  And by Baba et al., [16] is that the primary star (Be star) has an  $H\alpha$  emission line while the companion has an  $H\alpha$  absorption line.

Significant improvements in technological innovation over the past several years have brought the hardware to compensate perturbations in the wavefronts in real time [17, 18]. This active approach, known as adaptive optics (AO) system has advantages over a passive approach that are limited by noise. It is able to recover near diffraction limited images and improves the point source sensitivity. One of its most successful applications in astronomy has been in imaging of Neptune's ring arcs. AO systems are employed in other branches of physics as well. Liang et al. [19] have constructed a camera equipped with adaptive-optics that allows one to image a microscopic size of single cell in

the living human retina. They have shown that a human eye with adaptive-optics correction can resolve fine gratings that are invisible to the unaided eye. AO systems are useful for spectroscopic observations, as well as for photon-starved imaging with future very large telescopes, and ground based long baseline optical interferometers [20, 21].

In depth study has been made by Sirohi [22-24] on speckle metrology dealing with the coherent monochromatic source for over a period of two decades, and a few glimpses of such exemplary works can be witnessed in his recently published article [24]. Since I am familiar with the subject [25] that he was working on, I begin the paper with the discussions on the formation of speckles in the case of non-coherent quasi monochromatic source and of ways to detect them. Prior to this, a brief introduction on the behavior of the atmosphere and its effect on the plane wavefront from a stellar source is presented. The benefit of short-exposure images over long exposure is highlighted with emphasis set on their comparison as well. The data processing methods that are implemented in our institute in order to decipher both Fourier modulus and Fourier phase are described. The salient features of the adaptive optics system are discussed. At last but not the least, I conclude the paper after a brief discussion on certain astrophysical problems that can be targeted using moderate sized telescopes available in India, such as 2.34 meter Vainu Bappu Telescope (VBT), Kavalur, 2 meter Himalayan Chandra Telescope (HCT), Hanley.

## 2. Atmospheric turbulence and Seeing

Due to the turbulence and the concomitant development of thermal convection in the atmosphere, the density of air fluctuates in space and time. According to the Kolmogorov's theory of fluid turbulence [26], when the Reynolds number exceeds some value in a pipe (depending on the geometry of the pipe), the transition from laminar flows to turbulent flows occurs. The dimensionless quantity Reynolds number is defined as  $v_0L/\nu$ , where  $v_0$  is the mean flow speed,  $L$  is the transverse size of the pipe and  $\nu$  is kinematic viscosity of the fluid. If  $L$  is taken as some characteristic size of the flow of atmosphere the result holds good for atmospheric case. When the kinetic energy of the air motions at a given length scale is larger than the energy dissipated as heat by viscosity of the air at the same scale - the kinetic energy of large scale motions would be transferred to smaller and smaller motions; motions at small scales would be statistically isotropic at the small scales, viscous dissipation would dominate the breakup process. The distribution of turbule sizes ranges from millimeters to meters, with lifetimes varying from milliseconds to seconds.

Heating of the Earth's atmosphere by solar radiation causes turbulent motions in the atmosphere. During day time, large warm packets of air closer to the ground move up due to buoyancy and initiate convection causing the turbulence near the ground. They dissipate their kinetic energy continuously and randomly into smaller and smaller packets of air, each having a unique temperature. These packets are called turbulent eddies. Convection changes with insolation and disappears during night time. However, horizontal circulation of air starts. An important property of eddies is that they exist in a variety of length scales and their distribution is random. There exists an upper limit,  $L_0$ , decided by the process that generates turbulence and a lower limit,  $l_0$ , decided by the size at which viscous dissipation overtakes the breakup process.

Turbulent air motions cause variations in the density, pressure, temperature and humidity of the air from one point to another. While the local temperature fluctuations of the air could be of the order of few hundredth of a degree throughout the atmosphere, fluctuations of a few tenths of a degree or more are typical in the lowest layer of the atmosphere. The temperature fluctuations in small patches of air cause changes in index of refraction. The power spectral density of these refractive index fluctuations follows a power law with large eddies having greater power [27]. The

refractive index of the atmosphere may be expressed as,

$$n(\mathbf{r}, \mathbf{t}) = n_0 + n_1(\mathbf{r}, \mathbf{t}), \quad (1)$$

where,  $n_0 \approx 1$  is the mean refractive index of air,  $n_1(\mathbf{r}, \mathbf{t})$  the randomly fluctuating term,  $\mathbf{r}$  the 3-dimensional (3-D) position vector and  $t$  the time. The refractive index varies due to the temperature inhomogeneities. The dependence of the refractive index of air upon pressure,  $P$  (millibar) and temperature,  $T$  (Kelvin), at optical wavelengths is given by [28],

$$n_1 \cong n - 1 = 77.6 \times 10^{-6} \frac{P}{T}. \quad (2)$$

As the refractive index of the air is highly sensitive to the temperature, it varies randomly from one point to another. Fluctuations in the refractive index induce random optical path lengths to the ray that are normal to the wavefront arriving at the top of the atmosphere from a distant star. Consequently, the wavefront reaches the external pupil of a ground based telescope, gets corrupted in the sense that the surface of constant phase is no longer planar; it has an overall tilt and small scale corrugations on top of it. The RMS value of the phase perturbations increases with the size of the wavefront.

The perturbations in the wavefront produce effects similar to optical aberrations in the telescope and thus degrade the image quality. When a very small aperture is used, a small portion of the wavefront is intercepted and the phase of the wavefront is uniform over the aperture. If the amplitudes of the small scale corrugations of the wavefront are much smaller than the wavelength of the light, the instantaneous image of a star is sharp resembling to the classical diffraction pattern taken through an ideal telescope, in which the point spread function (PSF) is invariant to spatial shifts. In the absence of the atmospheric turbulence, FWHM, known as Airy disk, is the diffraction limit of telescope, i.e.,  $\theta \sim \lambda/D$ , where  $\lambda$  is a wavelength of light and  $D$  the diameter of the telescope.

The discrete layers of turbulence are blown by wind across the telescope aperture, hence a change in tilt occurs, which in turn, causes random motion of the star's image at the focal plane. As the aperture size increases, there is a decrease in the sharpness and amplitude of the motion; the amplitude of the random variation of phase across the intercepted wavefront tends to become larger. This leads to the blurring of the image, which is larger than the Airy disk of the telescope. For a 2 meter telescope, the size of this Airy disk in the absence of the atmospheric turbulence, is 0.05 arcsec (") at  $0.5\mu\text{m}$ . While in the presence of such turbulence the size of the image becomes typically 0.5 - 2". The resolution at the image plane of a ground based telescope is dictated by the width of the PSF of both the atmosphere and the telescope, which is of the order of  $(1.22\lambda/r_0)$ , where  $r_0$  is the average size of the turbulence cell [1]. For a good site, the typical value of  $r_0 \sim 20$  cm, therefore, any telescope larger than  $r_0$  cannot provide better spatial resolution. The image motion and blurring together are referred to as atmospheric seeing or simply seeing.

Seeing is the total effect of distortion in the path of the light via different contributing layers of the atmosphere to the detector placed at the focus of the telescope [3, 4]. The major sources of image degradation predominantly comes from the surface layer, as well as from the aero dynamical disturbances in the atmosphere surrounding the telescope and its enclosure, namely, (i) thermal distortion of primary and secondary mirrors when they get heated up, (ii) dissipation of heat by the latter mirror, (iii) rise in temperature at the primary cell, (iv) at the focal point causing temperature gradient close to the detector etc. Degradation in image quality can occur due to opto-mechanical aberrations such as aberrations in the design, manufacture and alignment of the optical train, mechanical vibrations of optical system as well.

Saha and Chinnappan [29] have computed the night time variations of  $r_0$  that varies at random at the 2.34 meter Vainu Bappu Telescope (VBT) site, Kavalur, India using the data obtained by

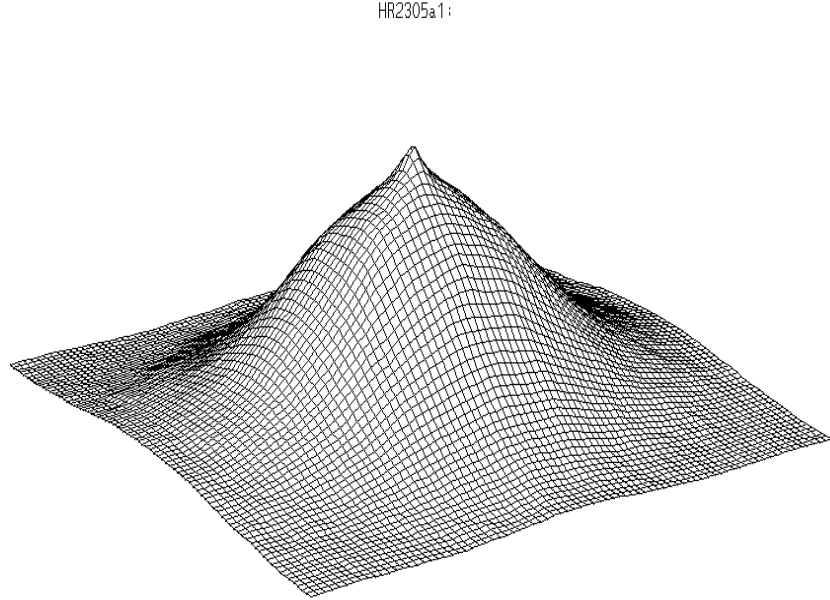


Figure 1: 3-D picture of the autocorrelation of HR 2305 observed at 2.34 m VBT, Kavalur, India, on 28 March 1991, at 1510 UT [29].

means of speckle imaging. The averaged autocorrelation of these images contains both the autocorrelations of the seeing disk, as well as of the mean speckle cell. It is the width of the speckle component of the autocorrelation that provides the information on the size of the object being observed. The form of transfer function,  $\langle |\hat{S}(\mathbf{u})|^2 \rangle$ , is obtained by calculating Wiener spectrum of the instantaneous intensity distribution from a point source. Figure 1 depicts the autocorrelation of HR 2305 observed at 1510 hrs UT, obtained at the Cassegrain focus of 2.34 m VBT, Kavalur, India [29]. They found that the average observed  $r_0$  is higher during the later part of the night than the earlier part, implying that the PSF has a smaller FWHM during the former period. This might indicate that the slowly cooling mirror creates thermal instabilities that decrease slowly over the night. Figure 2 depicts the night time variations of  $r_0$  at 2.34 meter VBT, Kavalur [29].

### 3. Speckle imaging

Ever since the development of the speckle interferometric technique by Labeyrie [2], it is widely used both in the visible, as well as in the infrared (IR) bands. The description of speckle interferometry, runs as follows.

#### 3.1 Speckle formation and statistics

The term, speckle, refers to the grainy structure observed when an uneven surface of an object is illuminated by a fairly coherent source. The formation of speckles stems from summation of coherent vibrations having different random characteristics. The statistical properties of speckle pattern depend on both the coherence of the incident light, as well as on the random properties of the medium. Depending on the randomness of the source, spatial or temporal speckles tend to

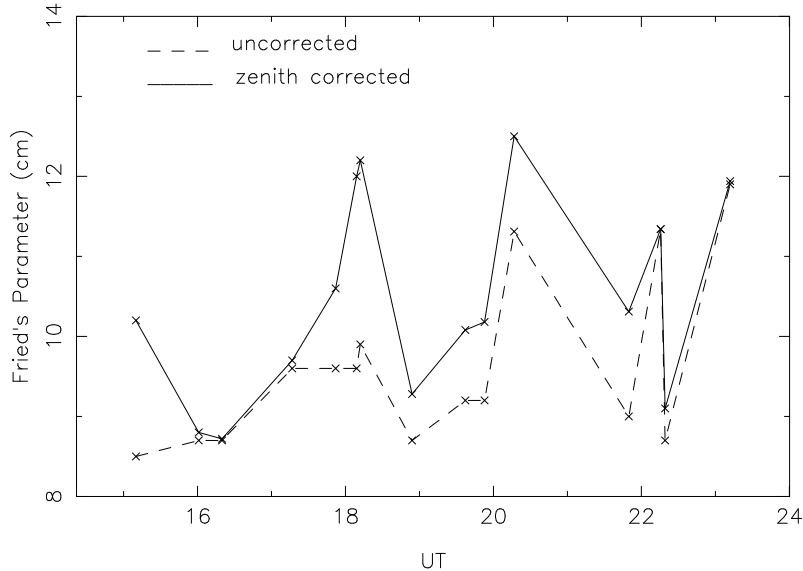


Figure 2: Nighttime variations of  $r_0$  at the 2.34 meter VBT, VBO, Kavalur [29].

appear; spatial speckles may be observed when all parts of the source vibrate at same constant frequency but with different amplitude and phase, while the latter are produced if all parts have uniform amplitude and phase. With a heterochromatic vibration spectrum, in the case of random sources of light, spatio temporal speckles are produced. Their statistical properties depend both on the coherence of the incident light and the random properties of medium. Since the positive and negative values cannot cancel out everywhere, adding an infinite number of such sine functions would result in a function with 100% constructed oscillations [30].

If a point source is imaged through the telescope by using the pupil function consisting of two subapertures ( $\theta_1, \theta_2$ ) corresponding to the two seeing cells separated by a vector  $\lambda u$ , a fringe pattern is produced with narrow spatial frequency bandwidth that moves within broad PSF envelopes with increasing distance between the subapertures, the fringes move with an increasingly larger amplitudes. The introduction of third aperture provides three pairs of subapertures and yields the appearance of three intersecting patterns of moving fringes. With  $r_0$  sized subapertures covering the telescope aperture synthesizes a filled aperture  $p_j$  (each pair of them,  $p_n, p_m$  separated by a baseline interferometer). The intensity at the focal plane  $I$ , according to the theory of diffraction [31] is determined by the expression,

$$I = \sum_{n,m} \langle \Psi_n \Psi_m^* \rangle, \quad (3)$$

The term  $\Psi_n \Psi_m^*$ , is multiplied by  $e^{i\psi}$ , where  $\psi$  is the random instantaneous shift in the fringe pattern. Each sub aperture is small enough for the field to be coherent over its extent. Atmospheric turbulence does not affect the contrast of the fringes but their phases are randomly distorted. If the exposure time is shorter than the evolution time of the phase inhomogeneities, then each patch of the wavefront with diameter  $r_0$  would act independently of the rest of the wavefront resulting in multiple images of the source. These sub images or speckles, as they are called and spread over the area defined by the long exposure image, can occur randomly along any direction within an angular

patch of diameter  $\lambda/r_0$ . The average size of the speckle is of the same order of magnitude as the Airy disk of the telescope in the absence of atmospheric turbulence.

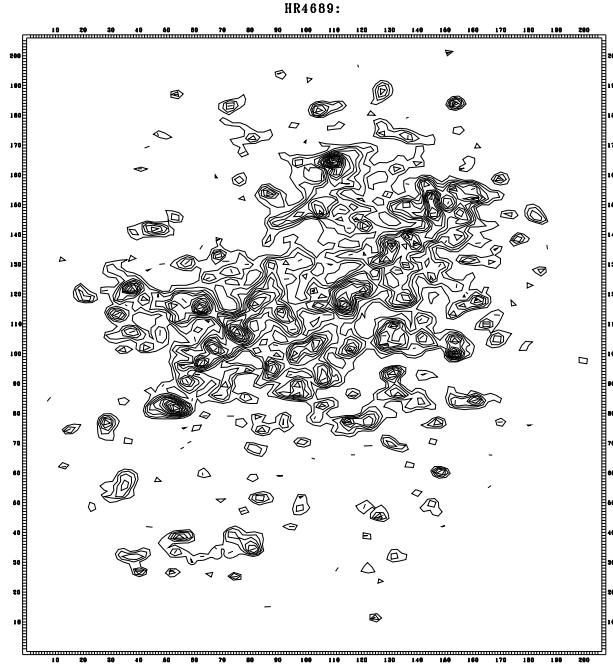


Figure 3: Specklegram of a binary star, HR 4689 obtained at VBT, Kavalur, India.

A specklegram of a point source is composed of numerous shortlived speckles. Constructive interference of the fringes would show an enhanced bright speckle. The number of correlation cells is proportional to the square of  $D/r_0$ , and the number of photons,  $N_p$ , per speckle, but is independent of its diameter. The lifetime of speckles is of the order of 0.1 to 0.01 seconds, and is determined by  $\tau_0 \approx r_0/\Delta v$ , in which  $\Delta v$  is the velocity dispersion in the turbulent seeing layers across the line of sight. Integration time of each exposure varies from a few milliseconds to twenty milliseconds, depending on the condition of seeing, to freeze the single realization of the turbulence.

### 3.2. Conventional image

The variance of phase difference fluctuations between any two points in the wavefront increases as the 5/3 power of their separation. When this variance exceeds  $\pi^2$  rad for some separation  $r_0$ , then all details smaller than  $\lambda/r_0$  will be obliterated in the long exposure images.

Figure 3 depicts the speckles of the star HR 4689; observations were carried out at 2.34 meter VBT, Kavalur, India with the speckle interferometer [32, 33]. A snap shot taken later would depict a different pattern but with similar probability of the angular distribution. A sum of similar exposures is the conventional image. It is easy to visualize that the sum of several statistically uncorrelated speckle patterns from a point source can result in an uniform patch of light a few arcseconds wide [34]. Figure 4 shows the result of summing 128 specklegrams demonstrating the destructions of finer details of the image by the atmospheric turbulence.

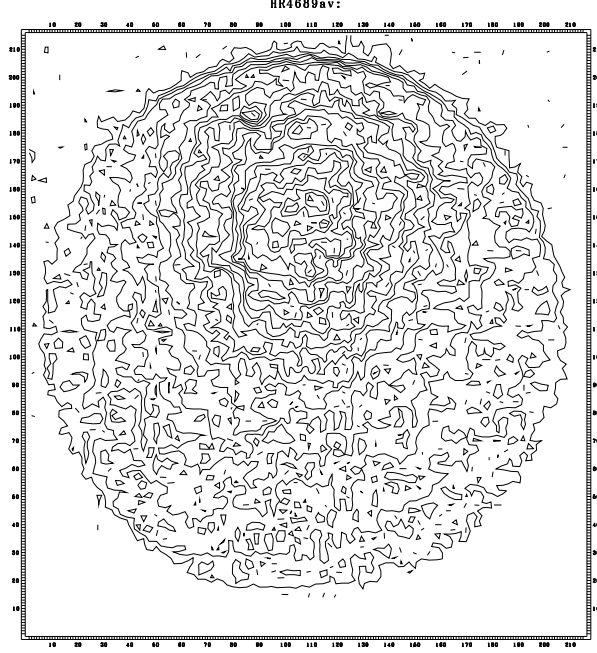


Figure 4: The result of summing 128 specklegrams of the same star, HR 4689.

The intensity distribution of the image,  $I(\mathbf{x})$ , is the convolution of intensity distribution of the object  $O(\mathbf{x})$  and the PSF,  $S(\mathbf{x})$ , i.e.,

$$\begin{aligned} I(\mathbf{x}) &= \int O(\mathbf{x}')S(\mathbf{x} - \mathbf{x}')d\mathbf{x}' \\ &= O(\mathbf{x}) \star S(\mathbf{x}), \end{aligned} \quad (4)$$

where  $\mathbf{x} = (x, y)$  is two dimensional (2-D) space vector, and  $\star$  stands for the convolution. The Fourier transform of this intensity  $I(\mathbf{x})$  is defined by,

$$\hat{I}(\mathbf{u}) = \int_{-\infty}^{\infty} I(\mathbf{x})e^{-i2\pi\mathbf{u}\cdot\mathbf{x}}d\mathbf{x}, \quad (5)$$

where  $\mathbf{u} = (u, v)$  the 2-D spatial frequency vector. In the case of the long exposure, the PSF is defined by its ensemble average,  $\langle S(\mathbf{x}) \rangle$ , and therefore, the average illumination,  $\langle I(\mathbf{x}) \rangle$  is given by,

$$\langle I(\mathbf{x}) \rangle = O(\mathbf{x}) \star \langle S(\mathbf{x}) \rangle, \quad (6)$$

where  $\langle \rangle$  indicates the ensemble average. By using 2-D Fourier transform (FT), this equation can be read as,

$$\langle \hat{I}(\mathbf{u}) \rangle = \hat{O}(\mathbf{u}) \cdot \langle \hat{S}(\mathbf{u}) \rangle, \quad (7)$$

where  $\hat{O}(\mathbf{u})$  is the object spectrum,  $\langle \hat{S}(\mathbf{u}) \rangle$  the transfer function of the atmosphere and the telescope for long exposure images.

### 3.3 Speckle interferometry

Speckle interferometry [2] estimates a power spectrum which is an ensemble average of the squared modulus of an ensemble of FT from a set of specklegrams that represent the resultant of diffraction-limited incoherent imaging of the object irradiance convolved with the function representing the combined effects of the turbulent atmosphere and the image forming optical system. An ensemble of such specklegrams,  $I_n(\mathbf{x})$ ,  $n = t_1, t_2, t_3, \dots, t_N$ , constitute an astronomical speckle observation. By integrating the autocorrelation function of these successive narrow bandpass exposures, the spatial resolution of the objects at low light levels can be obtained. The transfer function of  $S(\mathbf{x})$ , can be estimated by calculating Wiener spectrum of the instantaneous intensity from the unresolved star. The size of the data sets is constrained by the consideration of the signal-to-noise (S/N) ratio. Usually specklegrams of the brightest possible reference star are recorded to ensure that the S/N ratio of reference star is much higher than the S/N ratio of the programme star.

The variability of the corrugated wavefront yields speckle boiling and is the source of speckle noise that arises from difference in registration between the evolving speckle pattern and the boundary of the PSF area in the focal plane. These specklegrams have additive noise contamination,  $N_j(\mathbf{x})$ , which includes all additive measurement of uncertainties. This may be in the form of (i) photon statistics noise, and (ii) all distortions from the idealized isoplanatic model represented by the convolution of  $O(\mathbf{x})$  with  $S(\mathbf{x})$  that includes nonlinear geometrical distortions. Due to (i) variations of air mass or of its time average between the object and the reference, (ii) differences in seeing between the MTF for the object and its estimation from the reference (such a comparison is likely to introduce deviation in the statistics of speckles from the expected model based on the physics of the atmosphere), (iii) deformation of mirrors or misalignment while changing its pointing direction, (iv) bad focusing, (v) thermal effect from the telescope etc., the quality of the image degrades, which, in turn, would result either in the suppression or in the enhancement of intermediate spatial frequencies. This may lead to a dangerous artifact, yielding a wrong identification of the companion star [35]. Therefore, it is essential to choose the point source calibrator as close as possible for which all observing conditions are required to be identical to those for the object, preferably within  $1^\circ$  of the program star. The object and calibrator observations should be interleaved to calibrate for changing seeing condition by shifting the telescope back and forth during the observing run to equalize seeing distributions. Another difficulty arises from the non-detectability of a pair of photons closer than a minimum separation by the frame transfer CCD that is subjected to limitations in recording fast photon-event pairs, yielding a loss in high frequency information. This, in turn, produces a hole in the center of the autocorrelation – Centreur hole, resulting in the degradation of the power spectra or bispectra (Fourier transform of the triple correlation) of short exposures images.

For each of the short exposure instantaneous records, the instantaneous image intensity,  $I(\mathbf{x})$  is given by,

$$I(\mathbf{x}) = O(\mathbf{x}) \star S(\mathbf{x}) + N(\mathbf{x}), \quad (8)$$

In the Fourier plane, the effect becomes a multiplication, point by point, of the transform of the object,  $\hat{O}(\mathbf{u})$  with the transfer function,  $\hat{S}(\mathbf{u})$ , thus,

$$\hat{I}(\mathbf{u}) = \hat{O}(\mathbf{u}) \cdot \hat{S}(\mathbf{u}) + \hat{N}(\mathbf{u}). \quad (9)$$

The ensemble average of the power spectrum is given by,

$$\left\langle |\hat{I}(\mathbf{u})|^2 \right\rangle = |\hat{O}(\mathbf{u})|^2 \cdot \left\langle |\hat{S}(\mathbf{u})|^2 \right\rangle + \left\langle |\hat{N}(\mathbf{u})|^2 \right\rangle. \quad (10)$$

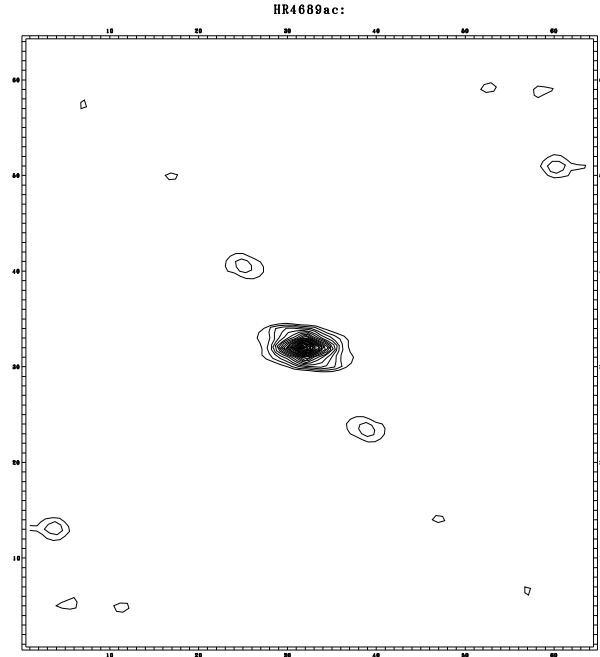


Figure 5: Autocorrelation of a binary star, HR 4689 [36]; the companion star is one of the contours that are symmetrically placed on either side of the main peak. The contours at the edge are the artifacts.

Saha and Maitra [36] developed an algorithm, where a Wiener parameter,  $w_1$ , is added to PSF power spectrum which helps reconstruction with a few realizations.

$$|\hat{O}(\mathbf{u})|^2 = \frac{\langle |\hat{I}(\mathbf{u})|^2 \rangle}{\langle |\hat{S}(\mathbf{u})|^2 \rangle + w_1}. \quad (11)$$

The speckle interferometry in the case of the components in a group of stars retrieves the separation, position angle with  $180^\circ$  ambiguity, and the relative magnitude difference at low light levels. Figure 5 depicts the autocorrelation of a binary system, HR 4689.

The programme of observing close binary systems (separation  $< 1''$ ) has been going on since 1996 using a speckle camera system (see Figure 6) at the Cassegrain focus of the 2.34 VBT, Kavalur, India [32, 33]. This camera system samples the image scale at the Cassegrain focus of the said telescope to  $0.015''$  per pixel of the intensified CCD. The wavefront falls on the focal plane and passes on to a microscope objective through a circular aperture of  $\sim 350 \mu\text{m}$  of an optical flat kept at an angle of  $15^\circ$ . The enlarged beam is recorded after passing through a narrow band filter by a Peltier cooled based solid state electron multiplying CCD based camera. Unlike the uncooled ICCD where data is stored in 8 bits, in this system, data is stored to 16 bits and can be archived to a Pentium PC. The surrounding star field of diameter  $\sim 10 \text{ mm}$  gets reflected from the optical flat on to a plane mirror and is reimaged on to an uncooled ICCD [37] for guiding the object.

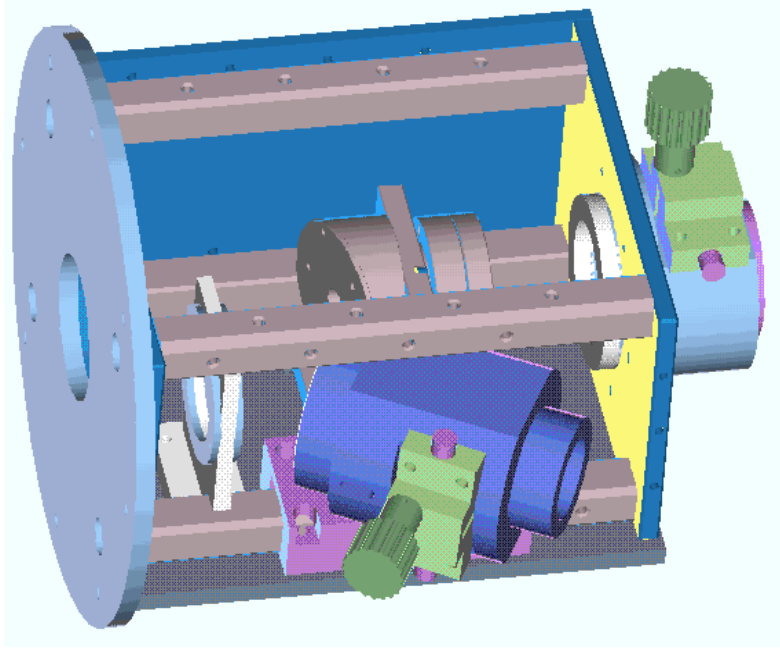


Figure 6: Overview of the Speckle camera system that is developed by Saha et al., [32, 33] for the use at VBT, Kavalur, India.

#### 4. Deciphering Fourier phase

Several algorithms have been developed to retrieve the diffraction limited phase of a degraded image, of which the triple correlation technique, known as speckle masking method [38, 39], is used by many observers. It is a generalization of closure phase technique where the number of closure phases is small compared to those available from bispectrum. The notable advantage of such an algorithm is that it is insensitive to (i) the atmospherically induced random phase errors, (ii) the random motion of the image centroid, and (iii) the permanent phase errors introduced by telescope aberrations; any linear phase term in the object phase cancels out as well. The images are not required to be shifted to common centroid prior to computing the bispectrum. The other advantages are: (i) it provides information about the object phases with better S/N ratio from a limited number of frames, and (ii) it serves as the means of image recovery with diluted coherent arrays [40]. The disadvantage of this technique is that it demands severe constraints on the computing facilities with 2-D data since the calculations are four dimensional (4-D). It requires extensive evaluation time and data storage requirements, if the correlations are performed by using digitized images on a computer.

A triple correlation is obtained by multiplying a shifted object,  $I(\mathbf{x} + \mathbf{x}_1)$  is multiplied with the original object,  $I(\mathbf{x})$ , followed by cross correlating the product mask,  $I(\mathbf{x})I(\mathbf{x} + \mathbf{x}_1)$  with the original one. The triple correlation of a specklegram is given by,

$$I(\mathbf{x}_1, \mathbf{x}_2) = \int_{-\infty}^{\infty} I(\mathbf{x})I(\mathbf{x} + \mathbf{x}_1)I(\mathbf{x} + \mathbf{x}_2)d\mathbf{x}, \quad (12)$$

where  $\mathbf{x}_j = \mathbf{x}_{jx} + \mathbf{x}_{jy}$  are 2-D spatial coordinate vectors. The Fourier transform of the triple

correlation is known as bispectrum. The ensemble averaged bispectrum is expressed as,

$$\widehat{I}(\mathbf{u}_1, \mathbf{u}_2) = \left\langle \widehat{I}(\mathbf{u}_1) \widehat{I}^*(\mathbf{u}_1 + \mathbf{u}_2) \widehat{I}(\mathbf{u}_2) \right\rangle, \quad (13)$$

$$= \widehat{O}(\mathbf{u}_1) \widehat{O}^*(\mathbf{u}_1 + \mathbf{u}_2) \widehat{O}(\mathbf{u}_2) \left\langle \widehat{S}(\mathbf{u}_1) \widehat{S}^*(\mathbf{u}_1 + \mathbf{u}_2) \widehat{S}(\mathbf{u}_2) \right\rangle, \quad (14)$$

where  $\mathbf{u}_j = \mathbf{u}_{jx} + \mathbf{x}_{jy}$ ;  $\widehat{I}(\mathbf{u}_j)$  and  $\widehat{I}^*(\mathbf{u}_1 + \mathbf{u}_2)$  denote Fourier transforms of  $I(\mathbf{x})$ , i.e.,  $\widehat{I}(\mathbf{u}_j) = \int_{-\infty}^{\infty} I(\mathbf{x}) e^{-i2\pi \mathbf{u}_j \cdot \mathbf{x}} d\mathbf{x}$ , and  $\widehat{I}^*(\mathbf{u}_1 + \mathbf{u}_2) = \int_{-\infty}^{\infty} I(\mathbf{x}) e^{-i2\pi (\mathbf{u}_1 + \mathbf{u}_2) \cdot \mathbf{x}} d\mathbf{x}$ . The object bispectrum is given by,

$$\widehat{O}(\mathbf{u}_1, \mathbf{u}_2) = \widehat{O}(\mathbf{u}_1) \widehat{O}^*(\mathbf{u}_1 + \mathbf{u}_2) \widehat{O}(\mathbf{u}_2) = \frac{\left\langle \widehat{I}(\mathbf{u}_1) \widehat{I}^*(\mathbf{u}_1 + \mathbf{u}_2) \widehat{I}(\mathbf{u}_2) \right\rangle}{\left\langle \widehat{S}(\mathbf{u}_1) \widehat{S}^*(\mathbf{u}_1 + \mathbf{u}_2) \widehat{S}(\mathbf{u}_2) \right\rangle}. \quad (15)$$

The bispectrum of a 2-D intensity distribution is a 4-D function. Due to this extension in to 4-D space it is possible that the phase information can survive. It is found experimentally [39] that the transfer function  $\langle \widehat{S}(\mathbf{u}_1) \widehat{S}^*(\mathbf{u}_1 + \mathbf{u}_2) \widehat{S}(\mathbf{u}_2) \rangle$ , is real and larger than zero up to the telescope cut off frequency. Due to the reality of this transfer function, the phase of the complex bispectra of the object is identical to the phase of the average bispectrum of the object specklegrams,

$$phase \left\langle \widehat{I}(\mathbf{u}_1, \mathbf{u}_2) \right\rangle = phase \left\langle \widehat{O}(\mathbf{u}_1, \mathbf{u}_2) \right\rangle. \quad (16)$$

Therefore phase information about the object can be obtained directly from the average bispectra without compensation of the transfer function. The measurement of the transfer function  $\langle \widehat{S}(\mathbf{u}_1) \widehat{S}^*(\mathbf{u}_1 + \mathbf{u}_2) \widehat{S}(\mathbf{u}_2) \rangle$ , may be calculated by evaluating specklegrams of an astronomical point source. Thus the object bispectrum is obtained from the equation (15), and the object triple correlation  $O(\mathbf{x}_1, \mathbf{x}_2)$  is obtained by inverse Fourier transforming of  $\widehat{O}(\mathbf{u}_1, \mathbf{u}_2)$ .

Another way is to evaluate the uncorrelated specklegram of the object (Gaussian speckle masking method), where no astronomical point source is essential to be measured. The advantage of this method over previous one is that it can be performed in the correlation domain as well as in Fourier domain. For a Gaussian model of the atmosphere [39].

$$\begin{aligned} & I(\mathbf{x}_1, \mathbf{x}_2 = \mathbf{s}) - I_{nmm}(\mathbf{x}_1, \mathbf{x}_2 = \mathbf{s}) - I_{nmm}(\mathbf{x}, \mathbf{x}_1 = \mathbf{s}) \\ & - I_{nmm}(\mathbf{x}_1, \mathbf{x}_2 = \mathbf{s}) + 2I_{nmk}(\mathbf{x}_1, \mathbf{x}_2 = \mathbf{s}) = O(\mathbf{x}_1, \mathbf{x}_2 = \mathbf{s}). \end{aligned} \quad (17)$$

Here different indices in  $I_{nmk}$  indicate that uncorrelated specklegrams are triple correlated. The equation (17) can be used to calculate the triple correlation  $O(\mathbf{x}_1, \mathbf{x}_2 = \mathbf{s})$  for any masking vector  $\mathbf{s}$ . If  $\mathbf{s}$  is selected suitably, a true image of the object can be obtained. In the case of complicated objects it is useful to choose a set of many different masking vectors in order to improve the signal to noise ratio. The information about suitable masking vectors is obtained from the object autocorrelation.

The image can be reconstructed by implementing recursive image reconstruction method in frequency domain, which is derived by assuming that a sampled version  $O_{p,q}$  of the object bispectra is available,

$$O_{p,q} = O_p \cdot O_q \cdot O_{-p-q} \quad p, q = -N \dots + N, \quad (18)$$

with  $\mathbf{u}_1 = p \cdot \Delta \mathbf{u}$ ,  $\mathbf{u}_2 = q \cdot \Delta \mathbf{u}$ , and  $P = -N \dots + N$ , where  $\Delta \mathbf{u}$  is a suitable sampling distance in the Fourier domain. In this method, the modulus and phase of the complex object bispectrum  $O_p$  are calculated separately. Therefore  $O_p$  is split in to:

$$O_p = |O_p| e^{i\psi_p}. \quad (19)$$

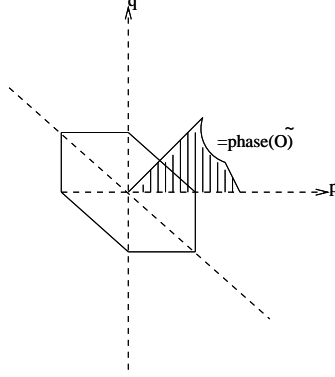


Figure 7: Complex bispectrum  $O_{p,q}$  of an object contains complete information about the modulus and the phase of the object spectrum  $|O_r|e^{(i\psi_r)}$ . The modulus information  $|O_r|$  can be reconstructed from one of the axes  $p = 0$ ,  $q = 0$  or  $p = q$ . The phase information  $e^{(i\psi_r)}$  is contained in the area in between these distinguished axes. Because of the eightfold symmetry of the bispectrum of a real function, only one octant of the bispectrum contains non-redundant information, as indicated by the area filled by lines.

In the recursive image reconstruction method the modulus of the object Fourier transform is obtained as in speckle interferometry. Speckle interferometry data are produced by setting  $p = 0$  (or equivalently by  $q = 0$  or  $p = -q$ ) in  $O_{p,q}$  i.e.,

$$O_{0,q} = O_0 \cdot O_q \cdot O_{-q} = \text{const.} |O_q|^2, \quad (20)$$

where the fact that the spectrum of a real object is Hermitian i.e.,  $O_q = O_{-q}^*$  is used. By substituting the equation (19) into (18) the phase of the complex spectrum of the object is reconstructed,

$$|O_{p,q}|e^{(i\psi_{p+q})} = |O_p|e^{(i\psi_p)} |O_q|e^{(i\psi_q)} |O_{-p-q}|e^{(i\psi_{-p-q})}. \quad (21)$$

For  $p + q = r$  and separate phase and modulus parts, the equation for phase will be,

$$e^{(i\psi_r)} = e^{[i(\psi_{r-q} + \psi_q - \beta_{r-q,q})]}, \quad (22)$$

where  $\beta_{r-q,q}$  is the phase of

$$O_{r-q,q} = |O_{r-q,q}|e^{(i\beta_{r-q,q})}. \quad (23)$$

From this equation the phase factors  $e^{(i\psi_r)}$  can be calculated recursively. It is sufficient to calculate  $O_r$  for positive  $r$  since  $O_r$  is Hermitian and therefore  $\psi_r = \psi_{-r}$ . By setting  $q = 1$  in the equation (22) yields

$$e^{(i\psi_r)} = e^{[i(\psi_1 + \psi_{r-1} - \beta_{r-1,1})]}, \quad (24)$$

where  $\psi_0 = \psi_1 = 0$ ,  $r = 2 \dots N$ .  $\psi_0$  is equal to zero because absolute position in the reconstructed image is of no interest. In order to explain this let us start the algorithm with  $r = 0$ . Both  $\psi_0$  and  $\beta_{0,1}$  are zero due to the reality of  $O(\mathbf{x})$  and  $O(\mathbf{x}_1, \mathbf{x}_2)$ . The recursive procedure is as follows,

$$\psi_2 = 2\psi_1 - \beta_{1,1} \quad (25)$$

$$\psi_3 = \psi_2 - \psi_1 - \beta_{2,1} \quad (26)$$

$$= 3\psi_1 - \beta_{1,1} - \beta_{2,1}$$

.....

$$\psi_r = r\psi_1 - \beta_{1,1} - \beta_{2,1} - \dots - \beta_{r-1,1}. \quad (27)$$

Apparently, the Fourier phase  $\psi_r$  and  $O_r$  can be determined from the phases of the bispectrum, except for the linear term  $r\psi_1$ . This unknown linear phase term corresponds to the unknown position of the object  $O(\mathbf{x} - \mathbf{x}_0)$ . For the reason explained above it is found that  $\psi_1$  remains undeterminable.

The recursion given in the equation (24) uses only the phase information contained in a single line ( $q = 1$ ) of the object bispectrum  $O_{p,q}$ . Additional phase informations can be obtained by setting  $q = 2 \dots N$  in the equation (22). Therefore each phase  $\psi_r$  has  $(r - 1)/2$  independent representations if  $r$  is odd and  $r/2$  representations if  $r$  is even. These different representations of the  $\psi_r$  can be averaged. To find the recursion formula, the equation (22) is used which is insensitive to noise because of summation,

$$e^{(i\psi_r)} = \text{const.} \sum_{0 < q \leq r/2} e^{[i(\psi_q + \psi_{r-q} - \beta_{r-q,q})]}, \quad (28)$$

where  $\psi_0 = \psi_1 = 0$  and  $r = 2 \dots N$  and the index  $q$  in the summation was selected such that all information contained in one octant of the object bispectrum is used to reconstruct the phases  $\psi_r$ . The remaining octants of the bispectrum do not supply additional information because of the inherent symmetry of bispectra as shown in Figure 7. By combining the phase factors with the modulus of the object Fourier transform (20), the recursive image is reconstructed. Inverse Fourier transform of the complex object spectrum yields the true image of the object.

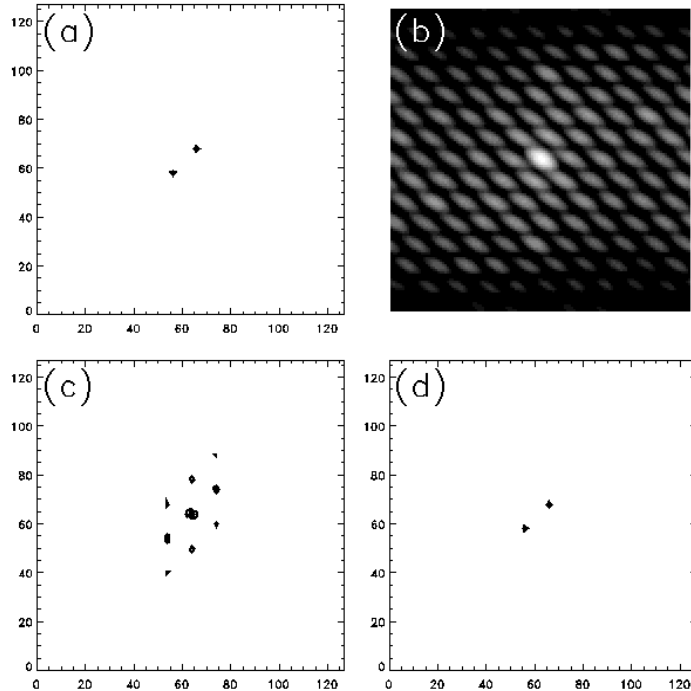


Figure 8: Fourier phase of a simulated binary system: (a) 2-D maps of a simulated binary system, (b) 2-D representation of its 4-D bispectrum, (c) its triple correlation and (d) its reconstructed image.

Saha et al., [41] have developed a code based on the unit amplitude phasor recursive reconstructor. The algorithm written in Interactive Data Language (IDL) takes about an hour for

processing 10 frames of size  $128 \times 128$  using the SPARC ULTRA workstation. The memory needed for the calculation exceeds 160 MB if the array size is more than the said number. Since the bispectrum is a 4-D function, it is difficult to represent it in a 3-D co-ordinate system. Therefore, the calculated values are stored in 1-D array and used them later to calculate the phase by keeping track of the component frequencies [41]. Assuming  $\psi(0, 0) = 0$ ,  $\psi(0, \pm 1) = 0$  and  $\psi(\pm 1, 0) = 0$ , the phases are calculated by the unitary amplitude method. Though the memory required is independent of the dimensionality of array, the time required to access an element in a 1-D array is much smaller than that in a 4-D array. In order to reduce the high frequency noise, Wiener filter parameter has been implemented in reconstruction stage. The bispectrum method has been tested with a computer simulated image by using a code developed by Saha et al. [41]. Figure 8 depicts (a) simulated binary system, (b) 2-D representation of a 4-D bispectrum, (c) triple correlation and (d) reconstructed image of the same binary system.

## 6. Adaptive optics

The adaptive optics systems (AO) remove the turbulence induced wavefront distortions by introducing controllable counter wavefront distortion which both spatially and temporally follows that of the atmosphere. The purpose of this system is to (i) sense the wavefront perturbations, and (ii) compensate for them in real time [42, 43].

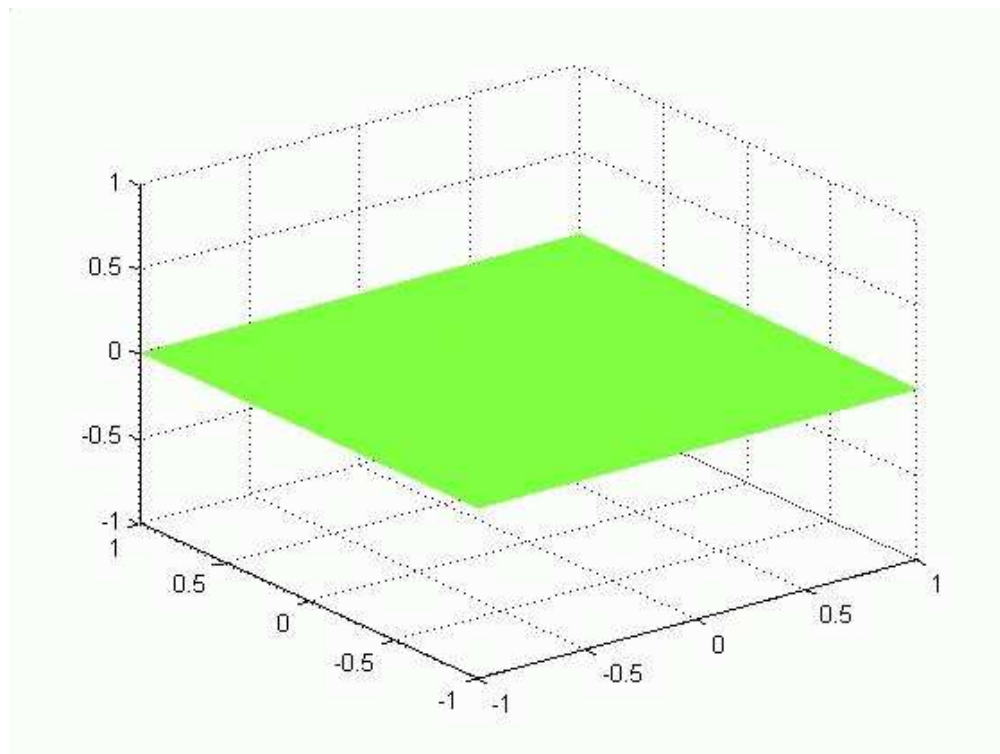


Figure 9: Plane wavefront recorded at the laboratory (Courtesy: V. Chinnappan). 3-D picture is generated by using Matlab.

As the wind moves the eddies past the telescope aperture, the tilt of the intercepted wavefront changes. Therefore, the wind velocity dictates the speed. In order to take a corrective measure, Greenwood [44] derives the mean square residual wavefront error as a function of servoloop bandwidth for a first order controller,

$$\sigma_{cl}^2 = \left( \frac{f_G}{f_{3db}} \right)^{5/3} \text{ rad}^2, \quad (29)$$

where  $f_{3db}$  is the closed loop bandwidth of the wavefront compensator and  $f_G = 0.426v/r_0$  the Greenwood frequency, in which  $v$  is the wind velocity in the turbulent layer of air.

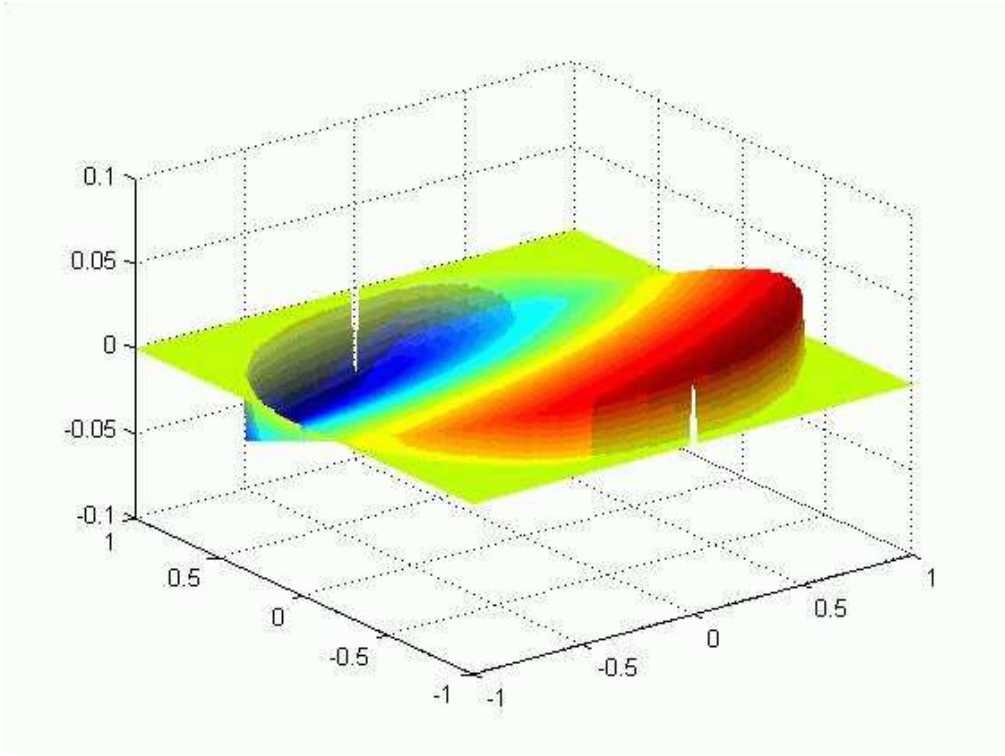


Figure 10: Laboratory measurement of wavefront tilt (Courtesy: V. Chinnappan).

Figure (9) depicts the plane wavefront that is generated at the laboratory with a laser source offering zero volt to the tip-tilt mirror. While Figure (10) depicts the wavefront tilt measured with the same source after applying one volt to the said mirror [45]. These images are grabbed by a CMOS imager based Shack-Hartman (SH) sensor. These plane and tilted wavefronts resemble to the wavefronts arriving to a detector from a distant star before and after passing through the turbulence of the atmosphere respectively. The laboratory experiment shows only tilt as a major error, while in the case of atmosphere, the wavefront will have complicated contours. Nevertheless, a reverse situation can be created by employing the AO systems in order to improve the throughput of the large telescope.

The required components for implementing an AO system are: (i) wavefront sensor, (ii) wavefront phase error computation and (iii) a flexible mirror whose surface is electronically controlled in real time to create a conjugate surface enabling to compensate the wavefront distortion [43, 46].

In order to remove the low frequency tilt error, generally the incoming collimated beam is fed by a tip-tilt mirror. After traveling further, it reflects off of a deformable mirror (DM) that eliminates high frequency wavefront errors (see Figure 11). A beam-splitter divides the beam into two parts: one is directed to the wavefront sensor to measure the residual error in the wavefront and to provide information to the actuator control computer to compute the DM actuator voltages and the other is focused to form an image. The control system acts as feedback loop; the next cycle corrects the small errors of the last cycle. This process should be at speeds commensurate with the rate of change of the corrugated wave-front phase errors.

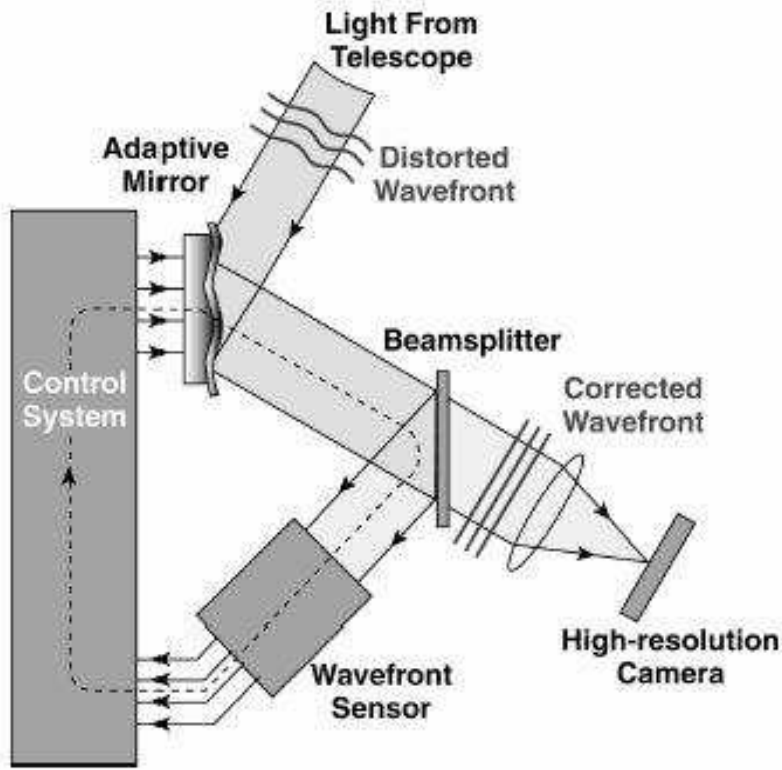


Figure 11: Schematic diagram of the adaptive optics system.

The shape of the image compensation devices is controlled such that perturbed incident wavefront phase-shifts are canceled as the optical field bounces from their surfaces. It is easier to achieve diffraction-limited information using AO systems at longer wavelengths since  $r_0 \propto \lambda^{6/5}$ , which implies that the width of seeing limited images,  $1.22\lambda/r_0 \propto \lambda^{-1/5}$  varies with  $\lambda$ . The number of degrees of freedom, i.e., the number of actuators on the DM and the number of sub-aperture in the wavefront sensor, in an AO system is determined by,

$$(D/r_0)^2 \propto \lambda^{-12/5}. \quad (30)$$

Another way to correct the disturbance in real time is usage of adaptive secondary mirror (ASM) that makes relay optics obsolete [47]. The other notable advantages are: (i) enhanced photon throughput that measures the proportion of light which is transmitted through an optical set-up,

(ii) introduction of negligible extra IR emissivity, (iii) causes no extra polarization, and (iv) non-addition of reflective losses [48]. Due to the interactor spacing, the resonant frequency of such a mirror may be lower than the AO bandwidth. The ASM system uses a SH sensor with an array of small lenslets, which adds two extra refractive surfaces to the wavefront sensor optical beam [49]. An  $f/15$  AO secondary with 336 actuators is installed on the 6.5 m Telescope of MMT observatory, Mt. Hopkins, Arizona. Figure 12 depicts the real time image of ADS 1585 [50] with a resolution of  $0.07''$  (FWHM). This image is acquired with the 6.5 m MMT adaptive secondary mirror at H Band ( $1.65 \mu\text{m}$ ).



Figure 12: Real time image of ADS 1585 [50](Courtesy: L. Close).

## 7. Summary

Speckle interferometry is a boon for the observational astronomy and has been contributing to the study of a variety of astrophysical problems. Among others the most important observations made by such technique is the discovery of compact cluster, R136a (HD 38268), of Doradus nebula in the Large Magellanic Clouds [14]. The object was thought to be the most massive star with a solar mass of  $\sim 2500M_{\odot}$ . In one of the IAU conferences, one full day was spent in discussing about its probability of a black hole [51]. The reconstructed image with speckle masking technique depicted more than 40 components in the  $4.9'' \times 4.9''$  field; the closest binaries were found to be  $0.03''$  and  $0.05''$  [52]. Recent observations with adaptive optics system by Brandl et al. [53] have revealed over 500 stars within the field of view  $12.8'' \times 12.8''$  covering a magnitude range of 11.2.

Studies of binary stars play a fundamental role in measuring stellar masses. Mass determinations of stars provide a benchmark for stellar evolution calculations. A long-term benefit of speckle imaging is a better calibration of the main-sequence mass-luminosity relationship. Speckle interferometric technique has made major inroads into decreasing the gap between visual and spectroscopic binaries by achieving angular resolution down to 20 milliarcsec (mas). Most measurements have been made at large aperture telescopes by groups in France, Russia, and the United States. Programmes of binary star interferometry are being carried out at telescopes of moderate and small aperture too. But measurements from the southern hemisphere continue to be rare. Many rapidly moving southern

binaries are being ignored and a number of discoveries are yet to be confirmed. Most of the late-type stars are available in the vicinity of sun. All known stars, within 5 pc radius from the sun are red dwarfs with  $m_v > +15$ . Due to the intrinsically faint nature of K- and M- dwarfs, their physical properties are not studied extensively. These dwarfs may often be close binaries which can also be detected. Figure 13 depicts the blind iterative deconvolution (BID) technique that applies to imaging in general which covers methods spanning from simple linear deconvolution algorithms to complex non-linear algorithms, reconstruction of a binary system, HR 5138 [54], in which the separation between the components is found to be about  $0.27''$ .

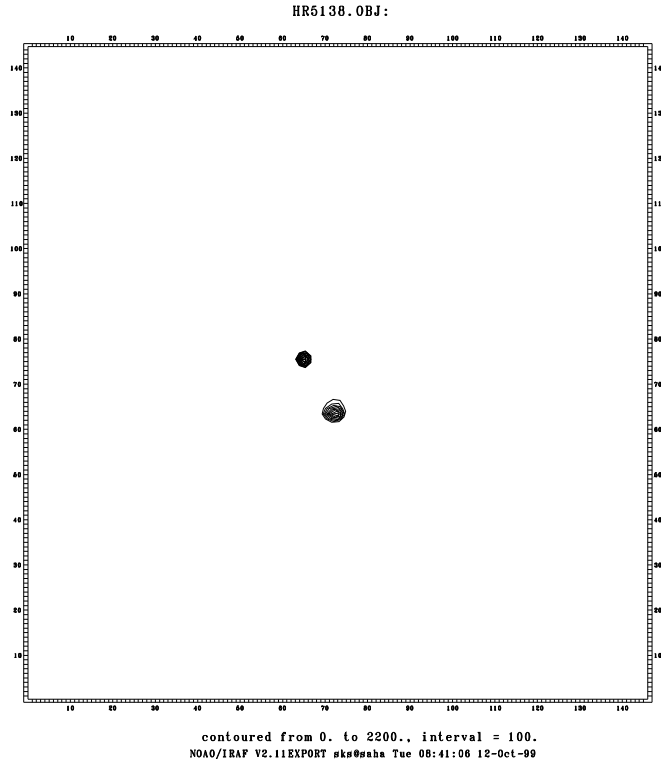


Figure 13: The blind iterative deconvolution (BID) reconstruction of a binary system, HR 5138 [54].

Another important field of observational astronomy is the study of the physical processes, viz., temperature, density and velocity of gas in the active regions of the active galactic nuclei (AGN); optical imaging in the light of emission lines on the sub-arcsecond scales can reveal the structure of the narrowline region. Binary black holes have been suggested to be the cause of the two components observed in the profiles of the broad emission lines of Arp 102 and a few other AGNs [55].

Another field of interest is the study of Quasars (QSO) that may be gravitationally lensed by stellar objects, viz., stars, galaxies, cluster of galaxies etc. located in the line of sight. The aim of the high angular imagery of those QSO's is to find their structure and components as well as to determine their number and structure as a probe of the distribution of the mass in the Universe.

The diffraction limited phase retrieval of a degraded image is an important subject that is being implemented in other branches of physics too, e.g., electron microscopy, wavefront sensing, and crystallography. A second-order moment (power spectrum) analysis provides only the modulus of

the object FT, whereas a third-order moment (bispectrum) analysis yields the phase allowing the object to be fully reconstructed. A more recent attempt to go beyond the third order, e.g., fourth-order moment (trispectrum), illustrates its utility in finding optimal quadratic statistics through the weak gravitational lensing effect [56], however, its implementation in optical imaging is a difficult computational task.

The programme of speckle imaging at VBT has been a successful one. Now we are in a position to obtain informations of Fourier phase of the objects too [41]. Mapping of the certain interesting objects, viz., active galactic nuclei, proto planetary nebulae will be undertaken in near future. However developing a school in the field of interferometry in optical/IR band in India is an important task to cope with the present day technological advancement across the globe. Several long baseline optical interferometers are in operation and made an impact in astrophysical studies [3, 4]. Work on a few interferometric projects by employing large telescopes are in progress. One such project called Large Binocular Telescope (LBT), in which the mirrors are co-mounted on a fully steerable alt-az mount, offers unprecedented spatial resolution of the order of 8-9 mas at  $\lambda \sim 1 \mu\text{m}$  [57]; the information in the  $u, v$  plane can be continuously combined or coadded. Developing a long baseline interferometer using such a technology will have far reaching impact on astrophysics, thus offering the possibilities for direct measurement of all the basic physical parameters for a large number of stars. With instruments as powerful as the current generation of working or planned interferometers, the element of serendipity will bring many surprises to astronomy.

**Acknowledgement:** I express my gratitude to Dr. L. Close for providing the real time image of ADS 1585.

## References

1. Fried D C, *J. Opt. Soc. Am.*, 56 (1966), 1972.
2. Labeyrie A, *Astron. Astrophys.*, 6 (1970), 85.
3. Saha S K, *Bull. Astron. Soc. Ind.*, 27 (1999), 443.
4. Saha S K, *Rev. Mod. Phys.*, 74 (2002), 551.
5. Hartkopf W I, McAlister H A, Mason B D, CHARA Contrib. No. 4, *Third Catalog of Interferometric Measurements of Binary Stars*, (1997) W.I.
6. Bonneau D, Labeyrie A, *Astrophys. J*, 181 (1973), L1.
7. Labeyrie A, Koechlin L, Bonneau D, Blazit A, Foy R, *Astrophys. J*, 218 (1977), L75.
8. Bonneau D, Foy R, *Astron. Astrophys.*, 92 (1980), L1.
9. Drummond J, Eckart A, Hege E, *Icarus*, 73 (1988), 1.
10. Saha S K, Rajamohan, Rao P V, Som Sundar G, Swaminathan R, Lokanadham B, *Bull. Astron. Soc. Ind.*, 25 (1997), 563.
11. Wood P, Bessel M, Dopita M, *Astrophys. J*, 311 (1986), 632.
12. Osterbart R, Balega Y, Weigelt G, Langer N, *Proc. IAU symp. 180*, eds., H Habing & G Lamers, (1996), 362.
13. Ebstein S, Carleton N P, Papaliolios C, *Astrophys. J*, 336 (1989), 103.
14. Weigelt G P, Baier G, *Astron. Astrophys.*, 150 (1985), L18.
15. Foy R, Bonneau D, Blazit A, *Astron. Astrophys.*, 149 (1985), L13.
16. Baba N, Kuwamura S, Miura N, Norimoto Y, *Astrophys. J.*, 431 (1994), L111.
17. Babcock H W, *Pub. Astron. Soc. Pac.*, 65 (1953), 229.
18. Rousset G, Fontanella J C, Kem P, Gigan P, Rigaut F, Léna P, Boyer P, Jagourel P, Gaffard J P, Merkle F, *Astron. Astrophys.*, 230 (1990), L29.
19. Liang J, Williams D R, Millar D T, *J. Opt. Soc. Am. A*, 14 (1997), 2884.

20. Labeyrie A, *Astrophys. J.*, 196 (1975), L71.
21. Mourard D, Bosc I, Labeyrie A, Koechlin L, Saha S, *Nature*, 342 (1989), 520.
22. Sirohi R S, editor, *Selected papers in Speckle Metrology*, (1991), Milestone Series MS 35, Bellingham, Washington, SPIE, Optical Engineering Press.
23. Sirohi R S, editor, *Speckle Metrology*, (1993), Dekkar, N Y.
24. Sirohi R S, *Contemporary Physics*, 43 (2002), 161.
25. Saha S K, *Ind. J. Phys.*, 73B (1999), 552.
26. Kolmogorov A, *Turbulence*, eds. S K Friedlander & L Topper, (1961), 151.
27. Tatarski V I, *Wave Propagation in Turbulent Medium*, (1967) Dover, N Y.
28. Ishimaru A, *Wave Propagation and Scattering in Random Media*, (1978), Academic Press, N Y.
29. Saha S K, Chinnappan V, *Bull. Astron. Soc. Ind.*, 27 (1999), 327.
30. Labeyrie A, *15th. Advanced Course, Swiss Society of Astrophys. and Astron.* ed.. A Benz, M Huber and M. Mayor, (1985), 170.
31. Born M, Wolf E, *Principles of Optics*, (1984), Pergamon Press.
32. Saha S K, Jayarajan A P, Sudheendra G, Umesh Chandra A, *Bull. Astron. Soc. Ind.*, 25 (1997), 379.
33. Saha S K, Sudheendra G, Umesh Chandra A, Chinnappan V, *Experimental Astronomy*, 9 (1999), 39.
34. Saha S K, Proc. *Young Astrophysicists of To-day's India*, (2001), <http://xxx.lanl.gov/astro-ph/0003125>.
35. Foy R, *Instrumentation for Ground Based Optical Astronomy - Present and Future*, (1988), ed. L. Robinson, Springer-Verlag, N Y, 345.
36. Saha S K, Maitra D, *Ind. J. Phys.*, 75B (2001), 391.
37. Chinnappan V, Saha S K, and Faseehana, *Kod. Obs. Bull.* 11 (1991), 87.
38. Weigelt G P, *Opt Communication*, 21 (1977), 55.
39. Lohmann A W, Weigelt G P, Wirnitzer B, *Applied Optics* 22 (1983), 4028.
40. Reinheimer T, Weigelt G P, *Astron. Astrophys.* 176 (1987), L17.
41. Saha S K, Sridharan R, Sankarasubramanian K, *Speckle Image Reconstruction of Binary Stars*, (1999), Presented at the XIX Astron. Soc. Ind. conf, Bangalore.
42. Beckers J M, *Annual Rev. Astron. Astrophys.* 31 (1993), 13.
43. Roggemann M C, Welsh B M, Fugate R Q, *Rev. Modern Phys.*, 69 (1997), 437.
44. Greenwood D P, *J. Opt. Soc. Am.*, 67 (1977), 390.
45. Chinnappan V, *Private Communication*, (2003).
46. Roddier F (editor), *Adaptive Optics in Astronomy*, (1999), Cambridge Univ. Press.
47. Bruns D, Barnett T, Sandler D, *SPIE.*, 2871 (1997), 890.
48. Lee J, Bigelow B, Walker D, Doel A, Bingham R, *Pub. Astron. Soc. Pac*, 112 (2000), 97.
49. Lloyd-Hart M, 2000, *Pub. Astron. Soc. Pac*, 112 (2000), 264.
50. Close L, <http://athene.as.arizona.edu/~lclose/AOPRESS/>, (2003).
51. Cassinelli J P, Mathis J C, Savage B R, *Science*, 212 (1911), 1497.
52. Pehlemann E, Hofmann K -H, Weigelt G P, *Astron. Astrophys.*, 256 (1992), 701.
53. Brandl B, Sams B J, Bertoldi F, Eckart A, Genzel R, Drapatz S, Hofmann R, Lowe M, Quirrenbach A, *Astrophys. J.*, 466 (1996), 254.
54. Saha S K, Venkatakrishnan P V, *Bull. Astron. Soc. Ind.*, 25 (1997), 329.
55. Ulrich M. -H., Proc. ESO-NOAO conf. *High Resolution Imaging Interferometry*, ed. F Merkle, Garching bei München, FRG, (1988), 33.
56. Hu W, <http://xxx.lanl.gov/astro-ph/0105117>, (2001).
57. Weinger P, *Private Communication*, (2001).